Efficient photocatalytic CO_2 reformation of methane on Ru/La-g-C_3N_4 by promoting charge transfer and CO_2 activation

Naixu Li,[a,c] Xianhe Li,[a] Rui Pan,[a] Miao Cheng, [a] Jie Guan,*[a] Jiancheng Zhou,[a] Maochang Liu,[b] Junwang Tang*[d], and Dengwei Jing,*[b]

[a] Prof. N. Li, X. Li, R. Pan, M. Cheng, Prof. J. Guan, Prof. J. Zhou
School of Chemistry and Chemical Engineering, School of Physics
Southeast University,
Nanjing, Jiangsu 211189, People's Republic of China
E-mail: guanjie@seu.edu.cn

[b] Prof. M. Liu, Prof. D. Jing
International Research Center for Renewable Energy, State Key Laboratory of Multiphase Flow in Power Engineering
Xi'an Jiaotong University,
Xi'an, Shaanxi 710049, People's Republic of China
E-mail: dwjing@mail.xjtu.edu.cn, maochangliu@mail.xjtu.edu.cn

[c] Prof. N. Li
Jiangsu Key Laboratory for Biomass Energy and Material
Nanjing, Jiangsu 210042, People's Republic of China
E-mail: naixuli@seu.edu.cn

[d] Prof. J. Tang
Department of Chemical Engineering
University College London
Torrington Place, London, WC1E 7JE, UK
E-mail: junwang.tang@ucl.ac.uk

Supporting information for this article is given via a link at the end of the document.

Abstract: Artificial photosynthesis, in which solar energy drives CO_2 to produce hydrocarbon fuels, is considered an effective way to solve the increasingly serious energy crisis and mitigate the greenhouse effect. Here, layered porous Ru-loaded and La-doped g-C_3N_4 nanosheets (Ru-LGCNs) were prepared by one-step Calcination, followed by in situ photoreduction deposition of Ru. The layered Ru-LGCN showed excellent photocatalytic CO_2 reformation of methane performance under visible light, and the generation rates of CO, CH_3CH_3, CH_3OH and $CH_3CH(OH)CH_3$ were 133, 154, 251 and 133 $\mu mol \cdot h^{-1}g^{-1}$, respectively. The reason for the enhanced photocatalytic activity of Ru-LGCN is the synergistic effect of bimetallic Ru and La. It is worth noting that the doped La can provide a good channel for charge transfer between LGCNs and CO_2. This change in the charge behavior of the transport path is beneficial to break the C=O bonds on the active site La and generate methyl radicals on Ru, resulting in the generation of C2+ hydrocarbons.

Introduction

The energy crisis, caused by the depletion of non-renewable fossil resources, and the environmental crisis, caused by the emission of greenhouse gas CO_2 from the burning of fossil fuels, have been recognized as the two most important global challenges for scientists in the past decade.[1-2] Therefore, driven by inexhaustible renewable energy of solar, the photocatalytic process is considered a way to convert greenhouse gas CO_2 into renewable high-value hydrocarbon fuels (such as CO, CH_3OH, CH_3CH_2OH). Thus, photocatalysis provides effective and attractive solutions to these crises. Initially, Inoue and co-workers reported the photocatalytic reduction and conversion of CO_2 on semiconductor photocatalysts, such as TiO_2, ZnO, CdS, GaP, and SiC, in 1979.[3] To improve the activity, durability, and selectivity of the photocatalytic reaction, scientists have made numerous attempts, including the design and synthesis of new photocatalysts and the construction of photocatalytic systems. Among them, the successful conversion of CO_2 using CH_4 as a reducing agent has received increasing attention in recent years.[4-6] For example, Shi and co-workers synthesized C_2H_6 and $CH_3CH_2OCH_3$ from a mixture of CO_2 and CH_4, using the Cu/CdS-TiO_2/SiO_2 composite photocatalyst at 373 K.[7] BalázsLászló and co-workers reported titanium nanotubes (TNTs) modified with gold and rhodium can effectively convert CO_2 and CH_4 into CO and H_2.[8] Tahir and co-workers also obtained similar results, replacing the photocatalyst with a Cu-modified g-C_3N_4 catalyst to produce CO/H_2 at 373 K.[9]

However, owing to the limitations of stable molecular bonds and multi-step reaction kinetics, the photocatalytic reaction efficiency has always been at a low level. Many strategies have been developed to overcome these challenges. In terms of energy band structure and electron-hole pair separation, element doping is the most effective method to improve the photocatalytic performance of GCN. Wang and co-workers found that potassium-doped g-C_3N_4 obtained effective visible light-driven

CO_2 reduction, and DFT calculations and XPS tests proved that potassium doping was interlayer doping, which changed the electronic structure of g-C_3N_4.[10] Yu and co-workers revealed that the reason for the enhanced performance of sulfur-doped g-C_3N_4 photocatalytic CO_2 reduction is that the band gap of g-C_3N_4 becomes narrower and the absorbance increases after doping the sulfur element.[11] Fu and co-workers prepared layered porous O-doped g-C_3N_4 nanotubes by continuous thermal oxidation stripping and cripping condensation of bulk g-C_3N_4 and showed excellent photocatalytic reduction performance of CO_2, due to the hierarchical structure of nanotubes and the O doping effect.[12] Among these dopant atoms, it is shown that the alkali metal atoms in g-C_3N_4 connect adjacent layers, increase the photogenerated carrier concentration, and further promote charge separation. In addition, through the intercalation of alkali metals and nitrogen species, a bidirectional channel is constructed between adjacent layers to reduce the potential barrier and guide the flow of charge to the desired location, that is, the reactive site. This allows the redox reaction to be separated in space, which not only reduces the annihilation rate of photogenerated carriers but also increases the rate of chemical reactions on the photocatalyst surface.

We recently reported that Zn-doped g-C_3N_4 photocatalyst can effectively convert CO_2 and methane to C2-hydrocarbons through photocatalytic reformation.[13] In particular, the Zn atom enters the g-C_3N_4 lattice, where it is chemically coordinated in the form of Zn-N bonds. The Zn-N bond can act as an electron channel, which accelerates the charge separation inside g-C_3N_4 and enables the rapid transfer of electrons from g-C_3N_4 to the co-catalyst of photodeposited Ru. Owing to the unique properties of ligand formation/coordination with other elements and the complex optical properties of trivalent lanthanide ions (La^{3+}), we incorporated lanthanide ions into carbon nitride.[14-16] The La element is introduced into the intermediate layer of carbon nitride to enhance charge transfer and photocatalytic activity through the interaction of La and the functional group of g-C_3N_4.

Herein, we successfully synthesized a series of Ru loaded and La-doped g-C_3N_4 (named Ru-LGCN) photocatalysts through continuous thermal oxidative exfoliation and condensation of urea and lanthanum salt, followed by in situ photoreduction deposition of Ru. The structural characteristics and physical-chemical properties of the photocatalysts were studied through DFT theoretical calculation, as well as CO_2-TPD, CH_4-TPD, PL, and BET tests. Then, the effects of La and Ru on the structure, morphology, and photocatalytic activity of g-C_3N_4 were discussed, and the mechanism of Ru-LGCN photocatalytic CO_2-CH_4 conversion was proposed.

Results and Discussion

As shown in Fig. 1, the successful synthesis of GCN and La-doped g-C_3N_4 was confirmed. The characteristic diffraction peaks of g-C_3N_4 near 13.1° and 27.4° were assigned to plane (100) for intra-planar structural packing and (002) plane for interlayer stacked conjugated aromatic structure of GCN, respectively. These assignments are consistent with previous literature

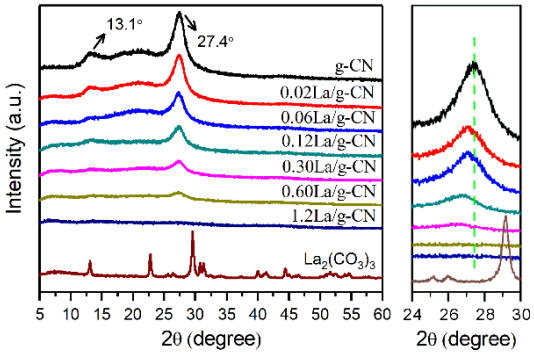

Figure 1. XRD patterns of GCN, nLGCN (n=0.12, 0.30, 0.40, 0.60, 0.80, 1.00) and $La_2(CO_3)_3$.

reports.[17-19] In the XRD pattern of La-doped GCN, with the continuous increase of La ions content, the (002) diffraction peaks gradually shift to a lower 2θ value. This indicates that the interstitial doping of La ions produces continuously enlarged interlayer distance.[20] The metal ions La^{3+} are doped into the nanocavities of g-C_3N_4, where they coordinate with the electron-donating N-containing functional groups of g-C_3N_4. Therefore, owing to the interaction between La and GCN and the release of NH_3 during the calcination process, La was successfully doped into the crystal.[21-22]

The TEM and SEM images containing information regarding morphologies and particle sizes are shown in Fig. 2. It can be seen that 0.6LGCN is composed of small nanosheets, which are uniform in size and shape compared with bulk g-C_3N_4. Fig. 2c shows that there is a disordered but well-developed 0.6LGCN pore system, with a pore size close to 20 nm. Fig. 2e illustrates the selected area electron diffraction pattern of the as-prepared nanocomposite, which indicates the crystalline structure of Ru nanoparticles. The lattice planes (101), (200), and (102) correspond to the crystalline lattice of Ru nanocrystals loaded on 0.6LGCN, which demonstrates the existence of Ru. The elemental mapping images of the samples, shown in Fig. 2f, reveal the uniform distribution of C and N elements in the catalyst, as well as O and La in the corresponding samples. In particular, the metal ions La^{3+} are uniformly distributed in the GCN matrix. This phenomenon is consistent with the XRD characterization results. The XRD pattern does not find the characteristic diffraction of lanthanum oxide or lanthanum carbonate.

The nitrogen adsorption–desorption isotherms and Barret–Joyner–Halenda (BJH) pore size distribution curves for samples LGCN and GCN are shown in Fig. 3. The results show that GCN has a classic IV type hysteresis loop, indicating the mesoporous structure (2–50 nm) of the sample. In addition, 0.6LGCN is classified as an H4 hysteretic loop according to the adsorption isotherm, which is attributed to adsorption-desorption in narrow slit pores. The isotherm can also be estimated from the BJH pore size distribution (2–25 nm).[23-24] The calculated pore diameter distribution curve shows that 0.6LGCN mesoporous distribution is narrow, and the maximum pore diameter radius is 25 nm. These data show that acetic acid lanthanum (III) can be used as a precursor to improve the specific surface area and porous structure. The reason for this result is that a large amount of NH_3 is released during the calcination process, and the gas escaping process increases the pore volume and dictates the pore size distribution, thus increasing the specific surface area. These

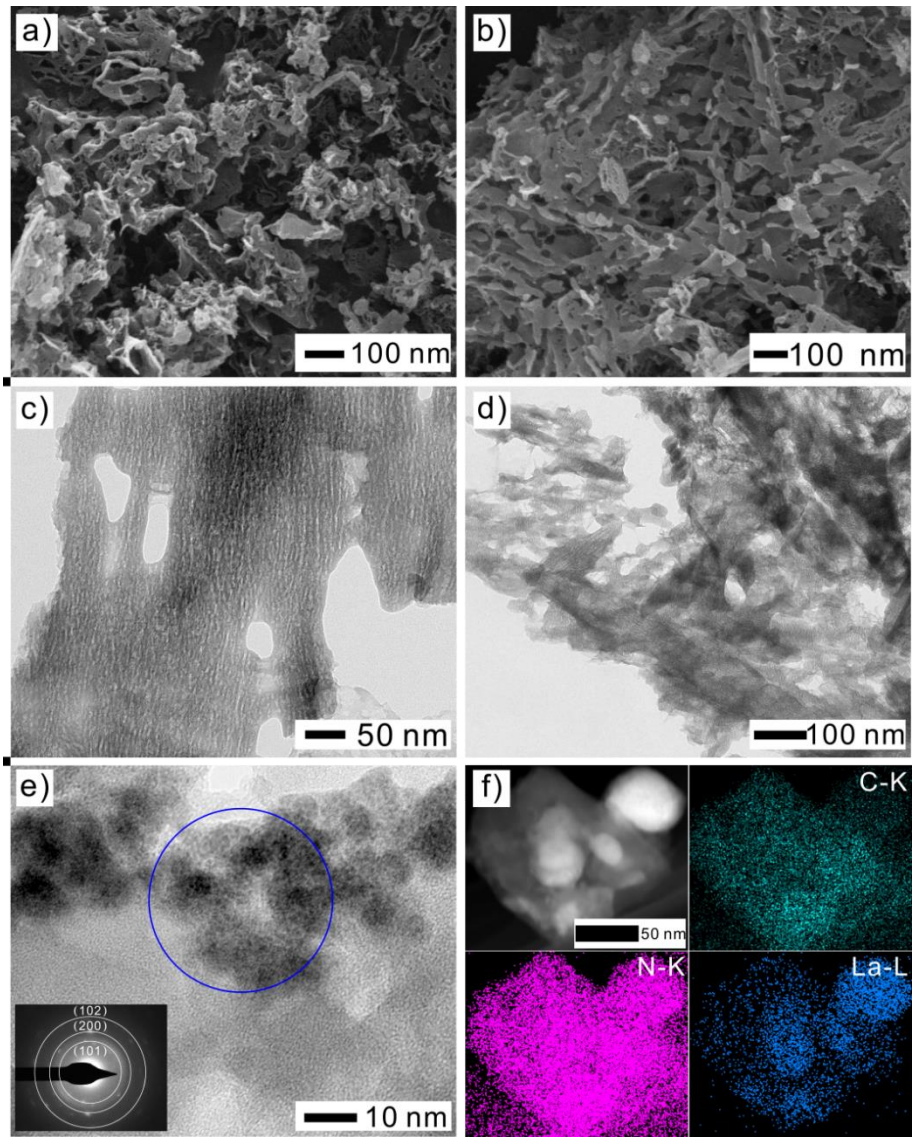

Figure 2. (a,b) SEM of g-C3N4 and 0.6LGCN, (c,d) TEM of 0.6LGCN and 0.5Ru-0.6LGCN and (e) HRTEM images of 0.5Ru-0.6LGCN and (f) SEAD pattern corresponding to the circled area in (e).

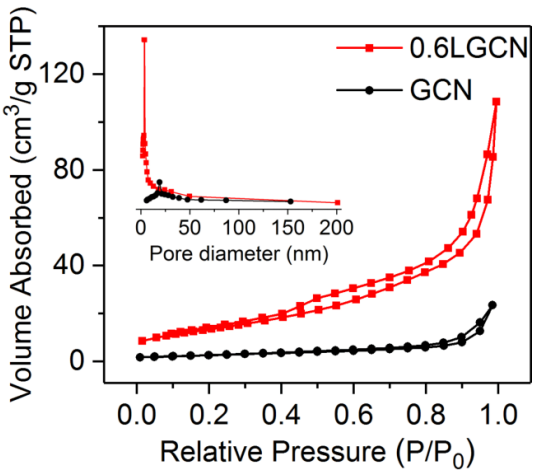

Figure 3. N_2 adsorption isotherms and pore size distribution curve of (a) GCN, (b) 0.6LGCN.

trends are observed in Fig. 2c. Similar results for other photocatalysts are summarized in Table 1. From Table 1, the addition of La precursors increased the specific surface area and pore size, reaching the maximum value at 0.12LGCN sample. Further increase in La precursors results in the decrease of specific surface area and pore size. The results show that a moderate amount of La doping is beneficial to the construction of more surface active sites, whereas a large amount of La doping may partially destroy the structure of g-C_3N_4, resulting in the reduction of its specific surface area. In addition, loading a small amount of Ru may cover the pore structure, resulting in a further reduction in surface area. The adsorption of CO_2 on the surface of the photocatalyst is the first step in the photocatalytic CO_2 reduction process. To evaluate the CO_2-capture ability of different catalysts, the CO_2 adsorption isotherms of GCN, 0.6LGCN and 0.5Ru-0.6LGCN was shown in Fig. S5. The results showed that La doping provides more CO_2 adsorption sites and the addition of Ru actually caused a slight decrease in the amount of CO_2 adsorbed.

Table 1. Specific surface area, pore volume, and pore diameter of pure GCN and La-doped LGCN samples.

Sample	S_{BET}/$m^2.g^{-1}$	V_{pore}/$cm^3.g^{-1}$	d_{pore}/nm
g-C_3N_4	12.9212	0.0336	17.02
0.12LGCN	58.8733	0.2575	12.94
0.30LGCN	56.7329	0.2400	12.18
0.40LGCN	53.1657	0.2110	10.92
0.60LGCN	49.0890	0.1779	9.49
0.80LGCN	37.9122	0.1312	7.11
0.5 Ru-0.60LGCN	45.1850	0.1562	9.18

As shown in Fig. S1, the FTIR spectra of pure GCN and nLGCN were recorded in the range of 500‑4000 cm^{-1}, and the detailed information of the organic structure was recorded. Several typical g-C_3N_4 absorption peaks were measured. The peak at 810 cm^{-1} can be attributed to the breathing mode of tri-s-triazine. The wide absorption near 3200 cm^{-1} is due to the stretching vibration of N-H bond. It is also worth noting that strong absorption occurs at 2166 cm^{-1}, compared to pure GCN, and increases with increasing La. This result corresponds to the suspended cyanide group (C ≡ N triple bond), one of the intermediates of urea pyrolysis. Several peaks between 1100 cm^{-1} and 1700 cm^{-1} can be attributed to the typical stretching pattern of the CN-heterocyclic system.[25-26]

To fully investigate the light absorption properties of as-prepared photocatalysts and thoroughly understand their optical structures, UV-vis, XPS, and PL spectra were recorded. Fig. 4a exhibits a sudden rise in absorption intensity from 450 nm up to the UV region for the GCN, which indicates a relatively narrow band gap of -2.73 eV. Additionally, intensive absorption peaks emerging in the UV region were attributed to the band gap between HOMO and LUMO in the polymeric melon units in accordance with other characterization results.[27] Meanwhile, a

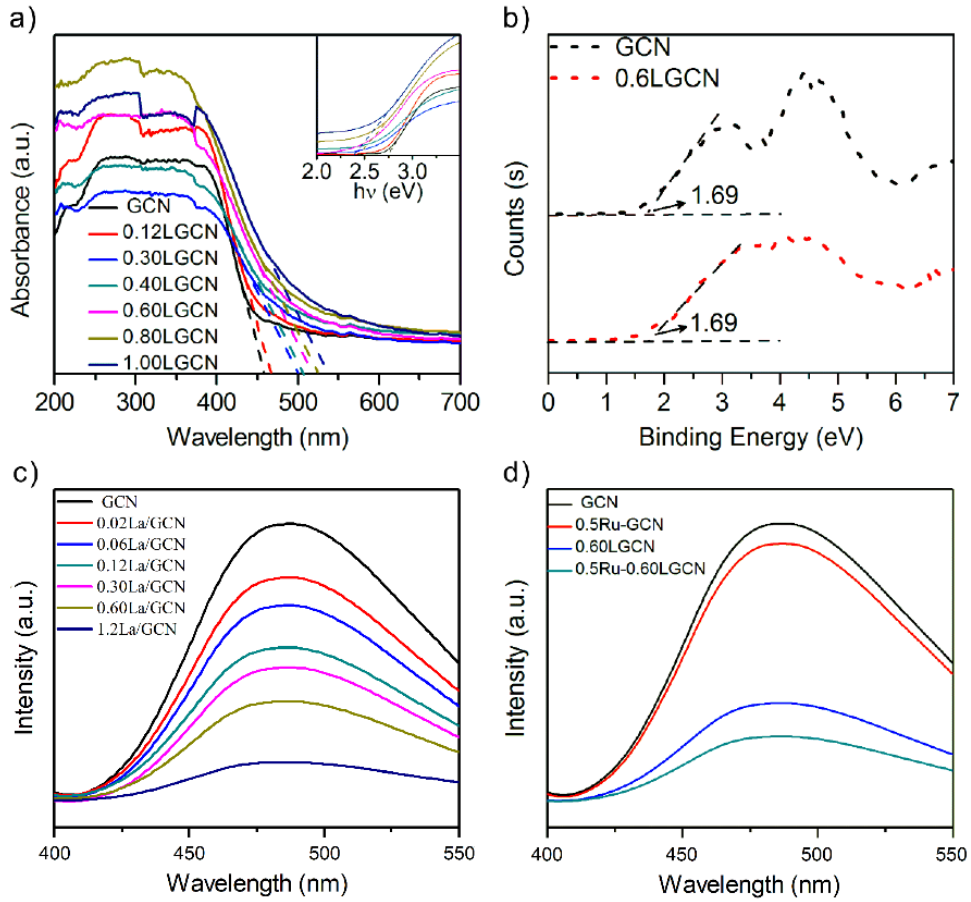

Figure 4. (a) UV-vis diffuse reflectance spectra of GCN and nLGCN. (b) XPS valence band spectra of GCN and 0.60LGCN. (c, d) PL spectra of different catalysts excited at 380 nm.

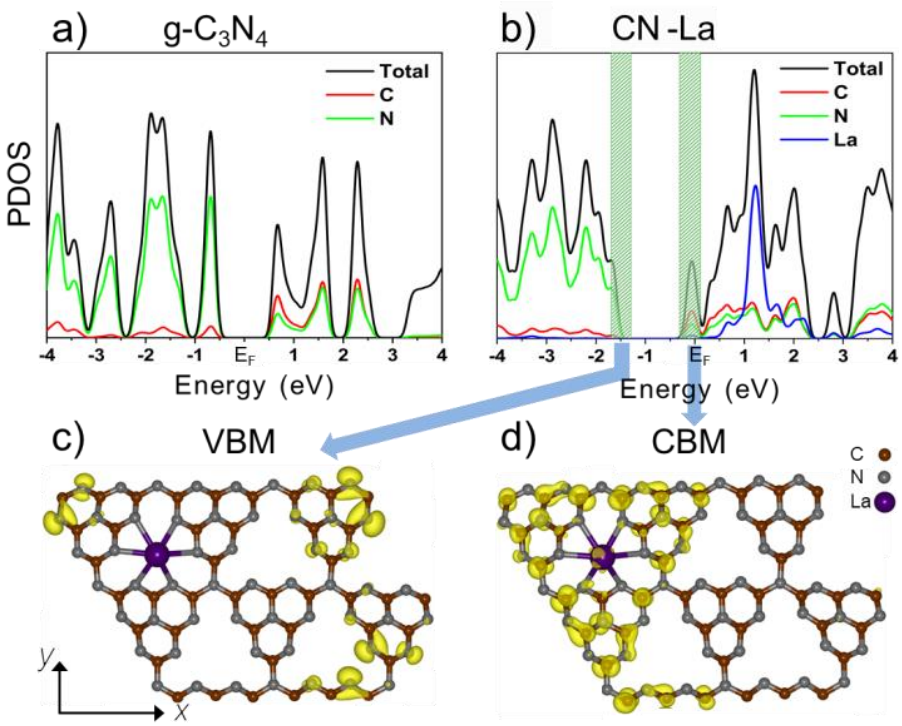

Figure 5. Electronic projected density of states (PDOS) of (a) g-C_3N_4 and (b) CN-La (LGCN) monolayers. Contributions of electrons from different elements are distinguished by color. Top view of partial charge density associated with frontier states in the (c) valence band (ρ_v) and (d) conduction band (ρ_c) for LGCN layer. The energy ranges associated with ρ_v and ρ_c are indicated by the green shaded region in (b) and extend from E_F− 1.7 eV < E < E_F− 1.3 eV for the valence band and E_F−0.3 eV < E < E_F+0.1 eV for the conduction band. The isosurface value for both is ρ_v and ρ_c is 4×10^{-3} eV/Bohr^3.

gradual red shift in the absorption edge of LGCN was observed after the introduction of La, indicating a narrower band gap. All band gaps, calculated using the Tauc equation and acquired via the intercept value of the tangent to the curve $(ahv)^2$ versus photon energy hv, are given in Fig. 4a.[26] As shown in Fig. 4b, The XPS valence band spectra of GCN and 0.6LGCN were tested to explore the influence of La doping on the valence band of the semiconductor photocatalyst. The test results showed that the valence band positions of GCN and 0.6LGCN were both 1.69 eV, so we speculated that the doping of La did not affect the valence band position. To more clearly prove the feasibility of CO_2 reforming, the energy band structure diagrams of GCN and 0.6LGCN were shown in Fig. S4. Therefore, the estimated calculation results implied that broadening the light response range and efficiently utilizing visible light can be achieved by doping La into GCN. A photoluminescence (PL) test (excited at 380 nm) was used to explain the migration, transfer, and recombination processes of the photogenerated electron-hole pairs in a semiconductor (Fig. 4c and d). Obviously, the PL spectrum intensity of LGCN photocatalyst decreased significantly, compared with that of GCN.[28] With the increase in La content, PL intensity gradually decreased, suggesting the possibility of carrier recombination can be reduced. It also indicates the photoinduced carriers can be appointed to a shorter distance, which needs to travel along with the C- and N-forming π-conjugated graphitic planes.[29-30] Similarly, the intensity of peaks decreased with the incorporation of metal Ru, which is due to the photogenerated charge transfer between the Ru and GCN.[31] Therefore, the synergy created by Ru and La is expected to favor the photocatalytic performance.

To better understand the electronic properties of La-doped g-C_3N_4 layer, the electronic projected density of states (PDOS) was calculated for g-C_3N_4 and LGCN. From Fig. 5a and b, the pristine g-C_3N_4 is a semiconductor with a band gap of 1.18 eV, which is underestimated by the DFT-PBE method. The La doping lowers the energy of both the valence and conduction bands in LGCN, and the doped structure displays a typically heavy n-doped electronic structure with E_F located at the bottom of the conduction band. To obtain a better impression of the nature of conducting states for the photogenerated carriers, the charge distribution associated with states at valence band maximum (VBM) and conduction band minimum (CBM) is depicted in Fig. 5c and d. Interestingly, the charge distribution for states at VBM and CBM located at separated regions on the layer. The CBM states are mainly contributed by electronic orbitals from La atom and neighboring C and N atoms, whereas the VBM states mainly contain orbitals from N atoms far from La atom. This result is consistent with the plotting of PDOS from different elements, as shown in Fig. 5b. The spatially separate states of VBM and CBM in LGCN can effectively prohibit recombination and promote the separation of photogenerated carriers. That is to say, the excited electrons will migrate to the CBM, which is located around the doped La atoms, and participate in the reduction of adsorbed CO_2. Simultaneously, the holes will migrate in the opposite direction to the VBM and participate in the oxidation process.

CO_2-TPD measurements were acquired to investigate the CO_2 adsorption/activation properties of the photocatalysts. CO_2-TPD curves of the samples are provided in Fig. 6a. For pure g-C_3N_4, two CO_2 desorption peaks, a strong peak at 128°C and a broad peak centered at around 500°C, were identified. The former

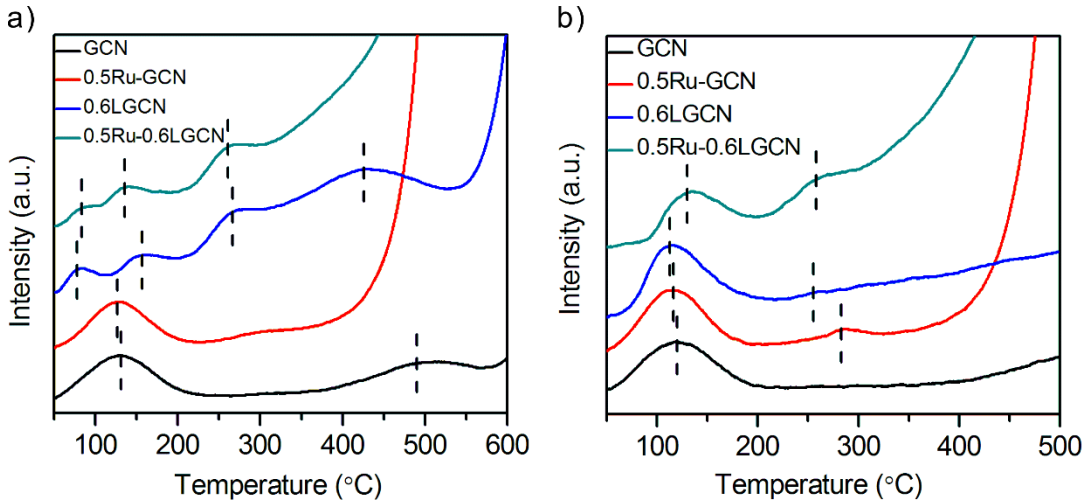

Figure 6. (a) CO_2-TPD curves and (b) CH_4-TPD curves of GCN, 0.5Ru-GCN, 0.6LGCN and 0.5Ru-0.6LGCN.

peak was attributed to desorption of CO_2 from weak basic site, probably $–NH_2$ sites, while the latter one could be assigned to chemical absorption sites with strong basicity. Moreover, three low-temperature peaks are located at approximately 80°C, 150°C, and 300°C for 0.5Ru-0.6LGCN and 0.6LGCN. It is suggested that a physical absorption peak under 100°C, a 150°C weak basic absorption corresponding to the species of bicarbonates, and a decomposition of carbonates peak at 265°C are collectively due to La in the lattice. Moreover, a similar strong basic site on 0.6LGCN was detected at 420°C, compared to the pristine GCN.[32-34] However, little difference was observed when loading Ru on the catalysts, which indicates little carbon dioxide is absorbed on the metal. Fig. 6b describes the CH_4 absorption performance of photocatalytic composites. The absorption temperatures below and above 200°C on the products correspond to weak and strong absorption of methane. Interestingly, the stability of the major absorption intensities of the composites at around 130°C reveals that a large proportion of CH_4 is attached to g-C_3N_4 by physical adsorption. In contrast to CO_2 curves, two middle absorption bumps stand out after depositing Ru on GCN and 0.6LGCN. This is likely attributed to partially absorbed CH_4 on the metal by chemisorption.[35]

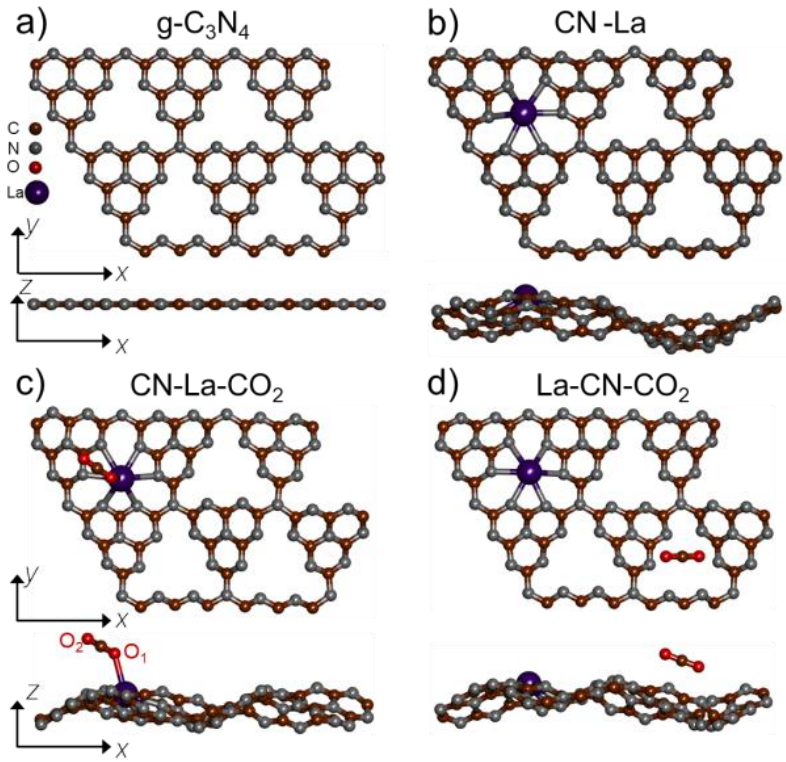

Figure 7. Top and side view of optimized structure for (a) pristine graphitic-carbon nitride (g-C_3N_4) monolayer, (b) La-doped g-C_3N_4 (LGCN), and the adsorption of CO_2 on CN-La (LGCN) (c) via the doped La atom and (d) without La atom. The O atom in CO_2 connected to La and the one far from the layer is distinguished by a subscript in (c).

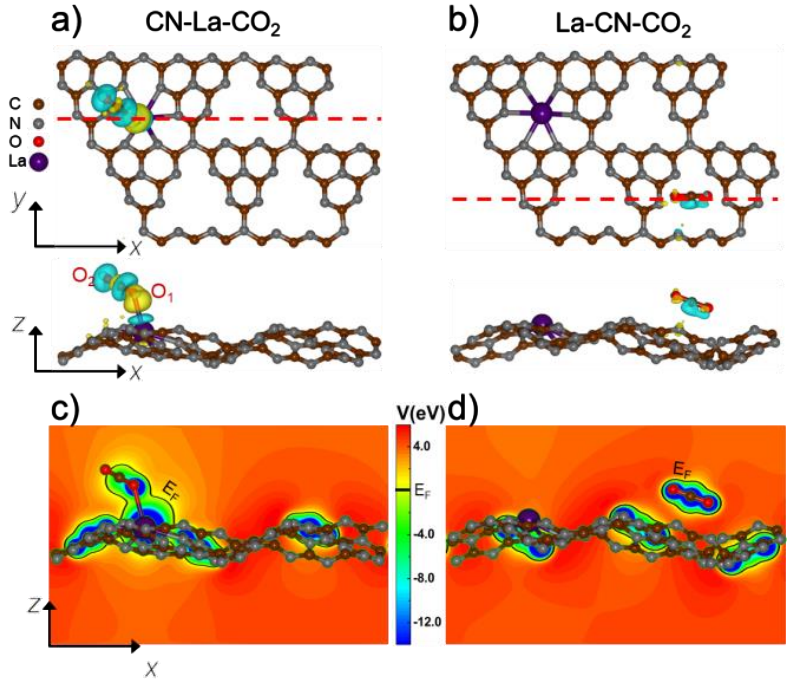

Figure 8. (a), (b) Differential charge density $\Delta\rho$ depicted by the isosurface bounding region of 9×10^{-4} eV/Å^3 in both top and side view and (c), (d) electrostatic potential V distributed in the xz-plane at the interface, superposed by the structural models, for CO_2 adsorbed on CN-La (LGCN) layer via La (left panel) and without La (right panel). The electron excess and deficiency are shown in yellow and blue, respectively, in (a) and (b). The location of the chosen xz-planes in (c), (d) are shown by the horizontal red dashed lines in the top view of (a), (b). The black solid lines represent the contour of Fermi level (E_F) in (c), (d).

Therefore, it facilitates the generation of long-chain products during CH_4 oxidation.

To verify the crucial role of the doped La atoms in enhancing the photocatalytic activity of g-C_3N_4, ab initio density functional calculations were executed to simulate the interaction between a CO_2 molecule and the La-doped g-C_3N_4 (LGCN) layer. The optimized structures for monolayers of pristine g-C_3N_4 and LGCN are shown in Fig. 7a and b. The most stable configuration for the doped La atom is inside one of the big C-N rings of g-C_3N_4. The doped structure becomes corrugated in the side view, compared to the flat 2D pristine structure. The adsorption of CO_2 on the LGCN surface via La atom doping and without La atom doping is compared, and the optimized structures are shown in Fig. 7c and d. When CO_2 is adsorbed near the La atom, the molecule is attached to the layer by connecting one O atom (O_1) to the La atom. However, when CO_2 is adsorbed far from the La atom, the molecule is adhered to the surface close to the center of the big C-N ring and almost parallel to the local plane. Our DFT calculations show that in the case of La doping, the La-O_1 bond length is about 2.759 Å, and the corresponding adsorption energy of one CO_2 molecule E_{ad}, which is defined as $E_{ad} = E_{tot}$(LGCN /CO_2) - E_{tot}(LGCN) - E_{tot}(CO_2), is -0.81 eV. In the case without La, however, the shortest distance from CO_2 to the LGCN layer is about 3.223 Å, and a lower value for E_{ad} of -0.56 eV is obtained. The larger E_{ad} in the case with La indicates the preference for CO_2 adsorbed on LGCN near the location of La atoms. The detailed results for the E_{ad} calculations are given in Table S1.

The electronic structure changes associated with the adsorption of CO_2 on the LGCN layer were calculated by DFT to further explore the effects of the doped La atoms on the charge transfer between LGCN and CO_2. The total charge density ρ for CO_2 adsorbed on the LGCN layer was shown in Fig. S6. The differential charge density $\Delta\rho$ = ρ(LGCN /CO_2) - ρ(LGCN) - ρ(CO_2) related to the assembly of CO_2 adsorbed LGCN layer from structures of only LGCN and only CO_2 was calculated. As depicted in Fig. 8a and b, the $\Delta\rho$ (visualized by contour plots) shows that when compared to the case without La, a much larger charge redistribution occurs near CO_2 when it is adsorbed on the layer via La. Additionally, there is a significant electron transfer to the O_1 atom from the other local atoms. Quantitative measurements for charge transfer using Bader charge analysis show that without La doping, each O atom in CO_2 gains about 1.063 electrons.[36-37] However, in the case with La doping, the O_1 atom gains 1.110 electrons and the O_2 atom gains 0.985 electrons. The extra electron flow to the O_1 atom caused by the La-O_1 bond can effectively modify the chemical activity of the adsorbed CO_2 molecule. The measurements for the bond length in CO_2 show that when attached to La, the length of the C-O_1 bond (1.187 Å) is larger than the C-O_2 bond (1.165 Å), while the values of the C-O bond length are approximately equal (1.175 Å and 1.177 Å) when adsorbed without La. The elongated C-O_1 bond indicates that the charge redistribution weakens the C-O_1 bond and enhances the activity of CO_2 adsorbed via La.

Since the charge transfer between the LGCN layer and CO_2 is restricted by the potential energy barriers, the regional electrostatic potential (V) in the adsorption region was investigated. The results for V distributed in the xz-plane at the interface, which is marked by the horizontal dashed line in the top view of Fig. 8a and b, are shown in Fig. 8c and d. The blue potential wells are caused by atoms close to the plane, and the high potential in red represents the vacuum region. When CO_2 is adsorbed on the LGCN layer without La, a potential barrier

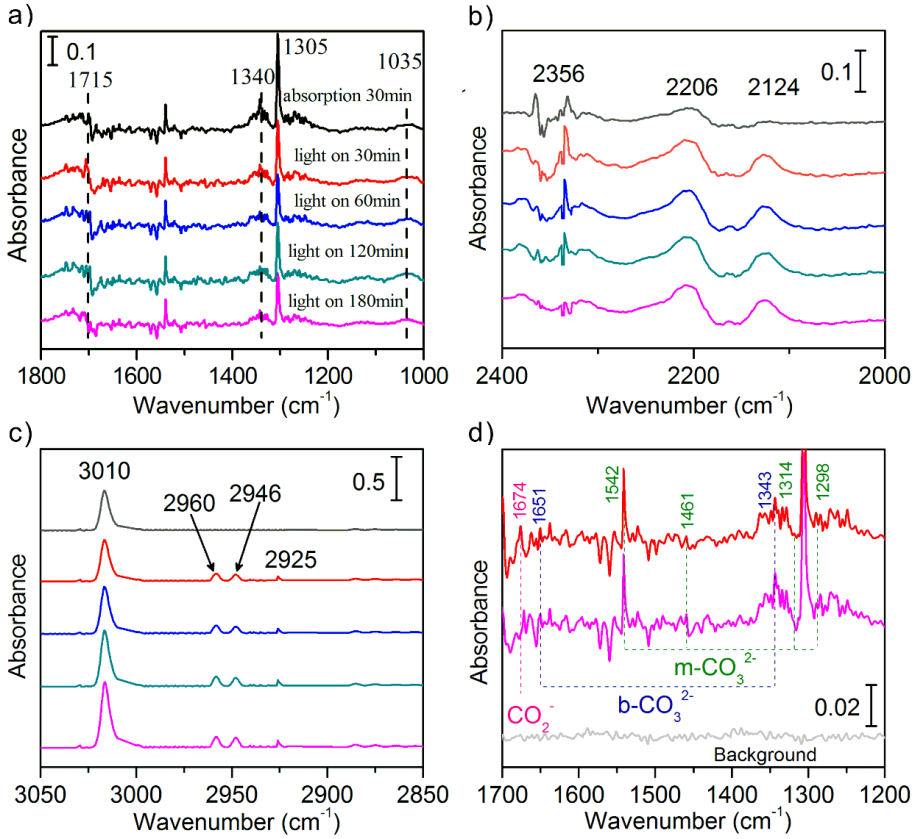

Figure 9. In situ FTIR spectra of the adsorbed species after introduction of CO_2 and CH_4 and irradiation for: i) 0 min, ii) 30 min, iii) 60 min, iv) 90 min, v) 120 min on 0.5Ru-0.6LGCN.

approximately 3.83 eV higher than the E_F was observed at the interface. This barrier is shown by solid black contours. The barrier much higher than E_F can dramatically hinder the charge transfer through the interface. However, when CO_2 is adsorbed via La, the potential barrier at the interface is significantly reduced to 2.42 eV lower than E_F. In this case, electrons at the Fermi level can easily migrate across the interface since the barrier is below E_F. These results show that the doped La can provide a good channel for charge transfer between LGCN and CO_2.

The XPS analysis for the synthesized catalysts was conducted to confirm the presence of C-N-La bonds. The La 3D high-resolution XPS spectrum (Fig. S3) of the purchased bare La_2O_3 sample exhibited peaks at 831.46 eV and 835.12 eV, as well as 848.25 eV and 852.37 eV, corresponding to the La $3d_{5/2}$ and La $3d_{3/2}$ states, respectively.[38] Compared to those of 0.6LGCN (Fig. S3), a negative shift in the binding energies suggests that electrons on La migrate to other atoms rather than O. It is further observed that in the high N 1s high-resolution XPS spectra (Fig. S2) of GCN and 0.6LGCN, a slight red shift indicates the electron density around the N atom is decreasing.[39-40] Thus, La tends to bind to N atoms. We also measured the XPS spectrum of Ru 3p. As shown in Fig. S3, a featured signal at 461.02 eV indicates Ru mainly existed in the zero-valence state. In addition, we also apply XPS analysis to Ru 3p of the composites after

Table 2. Product distribution involved in the controlled contrast experiments.

Sample	Condition	Rate of formation (μmol h^{-1} g^{-1})			
		CO	CH3CH3	CH3CH2OH	CH3CH(OH) CH3
none	UV-Vis & 100 °C	0	0	0	0
0.5Ru-0.6LGCN	Dark & 100 °C	0	0	0	0
GCN	UV-Vis & 100 °C	8.40	16.67	0	0
0.6LGCN	UV-Vis & 100 °C	66.67	125.02	0	0
0.5Ru-GCN	UV-Vis & 100 °C	13.13	15.69	0.65	5.00
0.5Ru-0.6LGCN	UV-Vis & 100 °C	133.33	153.68	130.38	133.33

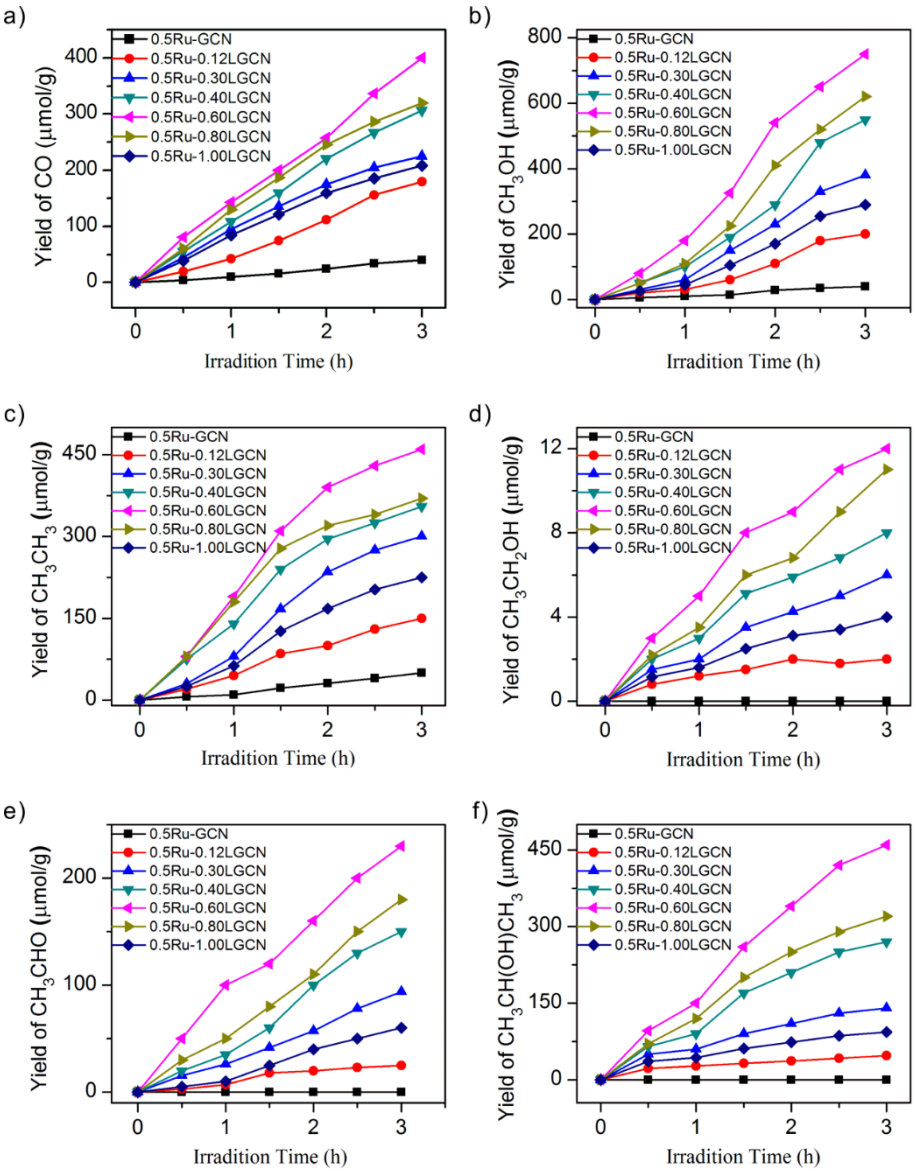

Figure 10. (a-d) Photocatalytic yield of the products over the various Ru-LGCN photocatalysts: (a) CO, (b) CH_3OH, (c) CH_3CH_3, (d) CH_3CH_2OH, (e) CH_3CHO, and (f) $CH_3CH(OH)CH_3$.

photoreaction (Fig. S3). No XPS peak shift was detected.

The paths and intermediates of photocatalytic CO_2 reforming of CH_4 were studied by in-situ FTIR spectra. Fig. 9 shows the in-situ FTIR spectra obtained by using 0.5Ru-0.6LGCN as photocatalyst with different irradiation time. The absorption peak located at near 1305 cm^{-1} was typical vibration absorption of methane, while the absorption peak near 2356 cm^{-1} was characteristic absorption of CO_2.[8, 41-42] It should be noted that the intensity of these absorption peaks decreased gradually after irradiation, and some new peaks appeared. More specifically, the characteristic vibration absorption peak at 2206 cm^{-1}can prove the presence of CO (C≡O) (as shown in Fig. 9b), and the intensity of the new absorption peak increases with the increase of irradiation time.[43] Specifically, as shown in Fig. 9a, the absorption peak at 1035 cm^{-1} was due to the vibration absorption of ν_s(C-O). The decrease of absorption peak intensity at 1340 cm^{-1} was caused by the vibration absorption of the ν_s(C=O) of decreasing CO_2. In addition, the vibration absorption is coincident with the absorption vibration of the methyl deformation mode around 1350 cm^{-1}. As shown in Fig. 9c, the wide bands of 3010 cm^{-1}, 2960 cm^{-1}, 2946 cm^{-1} and 2925 cm^{-1} were attributed to the vibration absorption of ν(C-H) of alkyl groups (*i.e.* $-CH_3$, $-CH_2-$, and -CH-). Interestingly, in the process of photocatalytic CO_2 reforming CH_4, the key CO_2 absorption existed in the dicentate carbonate (*i.e.* b-CO_3^{2-} and m-CO_3^{2-}) states, and the key transition state $\bullet CO_2^-$ (at 1674 cm^{-1}) was formed, as shown in Fig. 9d. The observation of $\bullet CO_2^-$ by the in-situ FTIR spectra showed that the activation of CO_2 in the form of CO_2 (carbonate) + e^- → $\bullet CO_2^-$ could be achieved by transferring photogenerated electrons to the CO_2 adsorption sites La. In Fig. 9a, the new absorption peak at ~1715 cm^{-1} corresponds to the characteristic absorption of δ (CHO). On the basis of the above analysis, the reaction mechanism of photocatalytic CO_2 reforming CH_4 to C2+ hydrocarbons on La doped g-C_3N_4 photocatalyst was described as the Equations (1) - (13).

$$0.5\mathrm{Ru}/0.60\mathrm{LGCN} + h\nu \rightarrow h^+ + e^- \quad (1)$$

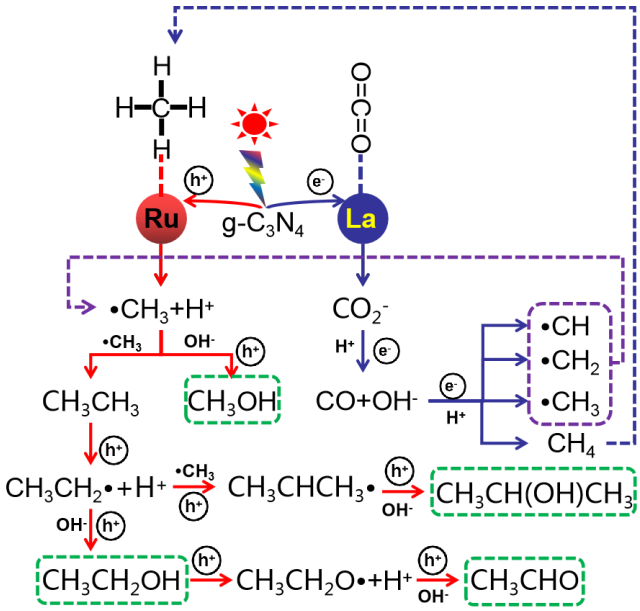

Scheme 1. main chemical reaction paths in the photocatalytic reaction process.

$$CH_4 + h^+ \rightarrow \cdot CH_3 + H^+ \quad (2)$$
$$CO_2 + e^- \rightarrow CO_2^- \quad (3)$$
$$CO_2^- + H^+ + e^- \rightarrow CO + OH^- \quad (4)$$
$$\cdot CH_3 + \cdot CH_3 \rightarrow CH_3CH_3 \quad (5)$$
$$\cdot CH_3 + OH^- + h^+ \rightarrow CH_3OH \quad (6)$$
$$CH_3CH_3 + h^+ \rightarrow CH_3CH_2 \cdot + H^+ \quad (7)$$
$$CH_3CH_2 \cdot + OH^- + h^+ \rightarrow CH_3CH_2OH \quad (8)$$
$$CH_3CH_2OH + h^+ \rightarrow CH_3CH_2O \cdot + H^+ \quad (9)$$
$$CH_3CH_2O \cdot + OH^- + h^+ \rightarrow CH_3CHO + H_2O \quad (10)$$
$$CH_3CH_2 \cdot + \cdot CH_3 + h^+ \rightarrow CH_3CHCH_3 \cdot \quad (11)$$
$$CH_3CHCH_3 \cdot + OH^- + h^+ \rightarrow CH_3CH(OH)CH_3 \quad (12)$$
$$H^+ + OH^- \rightarrow H_2O \quad (13)$$

The 0.5Ru/0.6LGCN photocatalyst was stimulated by UV-Vis irradiation to produce photogenerated electrons (e^-) in the valence band and photogenerated holes (h^+) in the conduction band, respectively (as shown in Eq. (1)). Correspondingly, photogenerated electrons and holes played the major role in the REDOX process of photocatalytic CO_2 reforming of CH_4. Photogenerated holes participated in the oxidation reaction of CH_4 to generate methyl radical ($\cdot CH_3$) and H^+ at the same time (Eqs. (2), (3) and (4)).[8, 44] Here, two $\cdot CH_3$ radicals were coupled to form ethane (Eq. (5)). Methanol could be produced by coupling reaction of $\cdot CH_3$ radicals with OH^-(Eq. (6)). The ethane was further oxidized with the hole (h^+) to form $\cdot CH_2CH_3$ radicals and further reacted with OH^- to form ethanol. Acetaldehyde can be formed by the oxidation reaction of ethanol (Eqs. (8), (9) and (10)).[45] Two $\cdot CH_3$ radicals conjugated with CH radicals to form isopropyl radicals, which then reacted with OH^- to form isopropyl alcohol. Of course, the reaction of the $\cdot CH_2CH_3$ radical with the hole (h^+) and further coupling of the methyl radical could also obtain isopropyl radical and isopropyl alcohol (Eqs. (7), (11) and (12)). In addition, the main chemical reaction paths in the photocatalytic reaction process are summarized in Scheme 1.

The photocatalytic performance of Ru modified and La doped g-C_3N_4 photocatalyst for the photocatalytic CO_2 reforming of methane was investigated under simulated solar irradiation. Fig. 10a-f summarized the yields changed of various photocatalytic products with time. The products obtained by photocatalytic reforming mainly include CO, CH_3OH, CH_3CH_3, and $CH_3CH(OH)CH_3$, and the reaction paths were shown in Scheme 1. The results showed that the photocatalytic activity had an obvious volcanic relationship with the contents of La and Ru. The optimal yields of CO, CH_3OH, CH_3CH_3, and $CH_3CH(OH)CH_3$ were 401.03, 750.02, 460.56 and 460.12 μmol/g, respectively, for 3 h over 0.5Ru-0.6LGCN photocatalyst. As shown in Table 2, the control experiment showed that even if the reaction system temperature was 100°C, the photocatalytic reforming reaction could only be carried out in the presence of both photocatalyst and light irradiation. Therefore, the reaction of photocatalytic CO_2 reforming of CH_4 was carried out under photocatalysis, and the photons provided enough energy to generate photogenerated electrons and holes to activate the REDOX reaction. In order to verify the carbon source, no hydrocarbons were observed after a 3-hour reaction in pure nitrogen, ruling out the possibility of photocatalytic generation of hydrocarbons from carbon residues or adsorbed during the preparation of the photocatalysts. Finally, the stability of the 0.5Ru-0.6LGCN catalyst was tested, as shown in Fig. S7. The yields of productions did not change significantly after five-time cycled test.

Conclusion

Here, layered porous Ru-modified and La-doped g-C_3N_4 nanosheets (Ru-LGCNs) were prepared by continuous thermal oxidative exfoliation and condensation of urea and lanthanum salt, followed by in situ photoreduction deposition of Ru. The layered Ru-LGCN showed excellent photocatalytic CO_2 reformation of methane performance under simulated sunlight, and optimal yields of CO, CH_3OH, CH_3CH_3, and $CH_3CH(OH)CH_3$ were 401.03, 750.02, 460.56 and 460.12 μmol/g, respectively, for 3 h over 0.5Ru-0.6LGCN photocatalyst. The CO_2-TPD and CH_4-TPD tests and theoretical calculations show that the reason for the enhanced photocatalytic activity of Ru-LGCN is the synergistic effect of bimetallic Ru and La. The spatially separate states of VBM and CBM in LGCN can effectively prohibit the recombination and promote the separation of photogenerated carriers. That is to say, the excited electrons will migrate to the CBM which is located around the doped La atoms and participate in the reduction of adsorbed CO_2, while the holes will migrate in the opposite direction to the VBM and participate in the oxidation process. It is worth noting that the doped La can provide a good channel for charge transfer between LGCN and CO_2. This change in the charging behavior of the transport path is beneficial to break the C=O bond on the active site La and generate methyl radicals on Ru particles, resulting in the generation of series C2+ hydrocarbons.

Acknowledgements

This work was financially supported by the National Natural Science Foundation of China (No. 22078057, No. 21576050, No. 51602052 and No. 61704110), Fundamental Research Funds for the Central Universities of China (No. 3207045403, 3207045409, 3207022002A3), Foundation of Jiangsu Key Laboratory for Biomass Energy and Material (JSBEM202001), Priority Academic Program Development of Jiangsu Higher Education Institutions (PAPD), Zhongying Young Scholars of Southeast University,

Applied Basic Research Program of Suzhou (SYG202026), Postgraduate Research & Practice Innovation Program of Jiangsu Province (SJCX20_0014, SJCX20_0015), and Innovation Platform Project Supported by Jiangsu Province of China (6907041203).

Keywords: Photocatalytic • CO_2/CH_4 catalytic conversion liquid hydrocarbons • La doped g-C_3N_4

[1] A. Kubacka, M. Fernández-García, G. Colón, *Chem. Rev.* 2012, ***112***, 1555-1614.
[2] S. Xie, Y. Wang, Q. Zhang, W. Fan, W. Deng, Y. Wang, *Chem. Commun.* 2013, ***49***, 2451-2453.
[3] T. Inoue, A. Fujishima, S. Konishi, K. Honda, *Nature* 1979, ***277***, 637-638.
[4] K. R. Thampi, J. Kiwi, M. Grätzel, *Nature* 1987, ***327***, 506-508.
[5] W. Yu, D. Xu, T. Peng, *J. Mater. Chem. A* 2015, ***3***, 19936-19947.
[6] S. Zhu, S. Liang, J. Bi, M. Liu, L. Zhou, L. Wu, X. Wang, *Green Chem.* 2016, ***18***, 1355-1363.
[7] D. Shi, Y. Feng, S. Zhong, *Catal. Today* 2004, ***98***, 505-509.
[8] B. László, K. Baán, E. Varga, A. Oszkó, A. Erdőhelyi, Z. Kónya, J. Kiss, *Appl. Catal. B* 2016, ***199***, 473-484.
[9] B. Tahir, M. Tahir, N. A. S. Amin, *Appl. Surf. Sci.* 2017, ***419***, 875-885.
[10] S. Wang, J. Zhan, K. Chen, A. Ali, L. Zeng, H. Zhao, W. Hu, L. Zhu, X. Xu, *ACS Sustain. Chem. Eng.* 2020, ***8***, 8214-8222.
[11] K. Wang, Q. Li, B. Liu, B. Cheng, W. Ho, J. Yu, *Appl. Catal. B* 2015, ***176-177***, 44-52.
[12] J. Fu, B. Zhu, C. Jiang, B. Cheng, W. You, J. Yu, *Small* 2017, ***13***, 1603938.
[13] N. Li, Y. Li, R. Jiang, J. Zhou, M. Liu, *Appl. Surf. Sci.* 2019, ***498***, 143861.
[14] Y. Wang, X. Wu, W. Zhang, W. Chen, *J. Magn. Magn. Mater.* 2016, ***398***, 90-95.
[15] J. Shen, L.-D. Sun, C.-H. Yan, *Dalton Trans.* 2008, 5687-5697.
[16] F. Wang, X. Liu, *Chem. Soc. Rev.* 2009, ***38***, 976-989.
[17] S. Cao, J. Low, J. Yu, M. Jaroniec, *Adv. Mater.* 2015, ***27***, 2150-2176.
[18] P. Niu, L. Zhang, G. Liu, H. M. Cheng, *Adv. Funct. Mater.* 2012, ***22***, 4763-4770.
[19] D. Marton, K. J. Boyd, A. H. Al-Bayati, S. S. Todorov, J. W. Rabalais, *Phys. Rev. Lett.* 1994, ***73***, 118.
[20] S. Hu, F. Li, Z. Fan, F. Wang, Y. Zhao, Z. Lv, *Dalton Trans.* 2015, ***44***, 1084-1092.
[21] B. Yue, Q. Li, H. Iwai, T. Kako, J. Ye, *Sci. Technol. Adv. Mater* 2011, ***12***, 034401.
[22] X. Wang, W. Yang, F. Li, Y. Xue, R. Liu, Y. Hao, *Ind. Eng. Chem. Res.* 2013, ***52***, 17140-17150.
[23] M. Li, Y. Hu, C. Liu, J. Huang, Z. Liu, M. Wang, Z. An, *RSC Adv.* 2013, ***4***, 992-995.
[24] K. Bahranowski, A. Kielski, E. M. Serwicka, E. Wisła-Walsh, K. Wodnicka, *Microporous Mesoporous Mater.* 2000, ***41***, 201-215.
[25] Z. Ding, X. Chen, M. Antonietti, X. Wang, *ChemSusChem* 2011, ***4***, 274-281.
[26] A. Khan, U. Alam, W. Raza, D. Bahnemann, M. Muneer, *J. Phys. Chem. Solids* 2018, ***115***, 59-68.
[27] J. Xu, K.-Z. Long, Y. Wang, B. Xue, Y.-X. Li, *Appl. Catal., A* 2015, ***496***, 1-8.
[28] L. Yang, X. Liu, Z. Liu, C. Wang, G. Liu, Q. Li, X. Feng, *Ceram. Int.* 2018, ***44***, 20613-20619.
[29] X. Bai, L. Wang, Y. Wang, W. Yao, Y. Zhu, *Appl. Catal. B* 2014, ***152***, 262-270.
[30] Y. Li, Z. Wang, T. Xia, H. Ju, K. Zhang, R. Long, Q. Xu, C. Wang, L. Song, J. Zhu, *Adv. Mater.* 2016, ***28***, 6959-6965.
[31] L. Ge, C. Han, J. Liu, Y. Li, *Appl. Catal., A* 2011, ***409***, 215-222.
[32] L. Pino, A. Vita, F. Cipitì, M. Laganà, V. Recupero, *Appl. Catal. B* 2011, ***104***, 64-73.
[33] Y. Yan, Y. Dai, H. He, Y. Yu, Y. Yang, *Appl. Catal. B* 2016, ***196***, 108-116.
[34] Y. Yu, Y. M. Chan, Z. Bian, F. Song, J. Wang, Q. Zhong, S. Kawi, *Int. J. Hydrog. Energy* 2018, ***43***, 15191-15204.
[35] S. Y. Foo, C. K. Cheng, T.-H. Nguyen, A. A. Adesina, *J. Mol. Catal. A: Chem.* 2011, ***344***, 28-36.
[36] M. Yu, D. R. Trinkle, *J. Chem. Phys.* 2011, ***134***, 064111.
[37] G. Henkelman, A. Arnaldsson, H. Jónsson, *Comput. Mater. Sci.* 2006, ***36***, 354-360.
[38] Ö. Tuna, E. B. Simsek, *J. Environ. Chem. Eng.* 2020, ***8***, 104445.
[39] J. Tang, R. Guo, W. Pan, W. Zhou, C. Huang, *Appl. Surf. Sci.* 2019, ***467-468***, 206-212.
[40] R. Jin, S. Hu, J. Gui, D. Liu, *Bull. Korean Chem. Soc.* 2015, ***36***, 17-23.
[41] X. Chen, Y. Li, X. Pan, D. Cortie, X. Huang, Z. Yi, *Nat. Commun.* 2016, ***7***, 12273.
[42] Z. H. Cheng, A. Yasukawa, K. Kandori, T. Ishikawa, *Langmuir* 1998, ***14***, 6681-6686.
[43] Y. Liu, D. Shen, Q. Zhang, Y. Lin, F. Peng, *Appl. Catal. B* 2021, ***283***, 119630.
[44] S. Delavari, N. A. S. Amin, Appl. Energy 2016, 162, 1171-1185.
[45] M. Tahir, B. Tahir, N. S. Amin, Mater. Res. Bull. 2015, 63, 13-23.

Entry for the Table of Contents

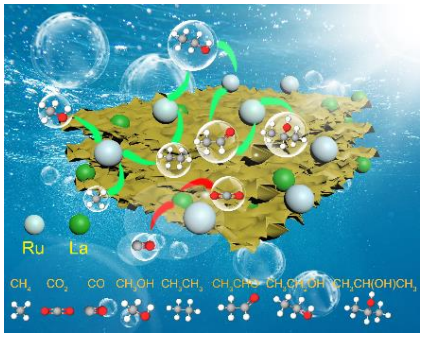

La doped g-C_3N_4 can provide a good channel for charge transfer between La and CO_2, which is consistent with theoretical calculations. This change of the charge behavior of the transport path is beneficial to break the C=O bond on the active site of La and generate methyl radicals o